Progress In Electromagnetics Research M, Vol. 23, 153–165, 2012

3D IMAGING METHOD FOR STEPPED FREQUENCY GROUND PENETRATING RADAR BASED ON COMPRESSIVE SENSING

J.-L. Cai[1,*], C.-M. Tong[1,2], W.-J. Zhong[1], and W.-J. Ji[1]

[1]Missile Institute, Air Force Engineering University, Sanyuan, Shanxi 713800, China

[2]State Key Laboratory of Millimeter Waves, Nanjing, Jiangsu 210096, China

Abstract—Long data collecting time is one of the bottlenecks of the stepped-frequency continuous-wave ground penetrating radar (SFCW-GPR). We discuss the applicability of the Compressive Sensing (CS) method to three dimensional buried point-like targets imaging for SFCW-GPR. It is shown that the image of the sparse targets can be reconstructed by solving a constrained convex optimization problem based on l_1-*norm* minimization with only a small number of data from randomly selected frequencies and antenna scan positions, which will reduce the data collecting time. Target localization ability, performance in noise, the effect of frequency bandwidth, and the effect of the wave travel velocity in the soil are demonstrated by simulated data. Numerical results show that the presented CS method can reconstruct the point-like targets in the right position even with 10% additive Gaussian white noise and some wave travel velocity estimation error.

1. INTRODUCTION

Ground Penetrating Radar (GPR) is an important remote sensing tool to detect the object buried in shallow ground and widely used in such areas as civil engineering [1], landmine detection [2], archeological investigations [3] and environmental applications [4], etc.

Generally speaking, there are two types of GPRs most commonly seen in literatures. One is (Carrier-Free Pulse CFP-GPR), which

Received 12 December 2011, Accepted 29 January 2012, Scheduled 8 February 2012

* Corresponding author: Ji-Liang Cai (shitouji840716@126.com).

images the subsurface by transmitting short electromagnetic (EM) pulses and processing the reflections due to permittivity discontinuities in the ground [5]. The other is the stepped-frequency continuous-wave GPR (SFCW-GPR) [6–9]. When it works, a stepped frequency signal probes the environment with a discrete set of frequencies. Compared with CFP-GPR, SFCW-GPR has several advantages, such as greater measurement accuracy, greater dynamic range, lower noise, easier frequency band and frequency steps selecting [9]. Therefore, it is becoming increasingly popular. In [6–8], SFCW-GPR is used to image buried landmines and objects.

Although SFCW GPRs have very good properties, they are not used widely in commercial systems. One important reason for this is long data acquisition time [9]. There are tens of scan positions and hundreds of measurements at each scan position, which means large quantities of data and long measurement time and thus make it too slow for some applications.

Compressive sensing (CS), proposed by Donoho [10], shows that certain signals and images, which are sparse or compressible in some domains such as time, space and frequency, can be recovered with far fewer samples or measurements than traditional Nyquist sampling theorem. Due to its compressed sampling and exact reconstruction ability, CS has been widely used in radar field imaging [11], such as Ground Penetrating Radar (GPR) [9, 12], through-wall radar imaging [13], SAR [14], and ISAR imaging [15]. In recent years, CS has received more and more attention in radar applications, for lightening up sampling burden and improving the resolution of radar system.

In [12], a 3D GPR imaging method based on CS is proposed. The target space is reconstructed from just a few compressive sensing data obtained by random aperture measurements. However, it is an impulse GPR. In [9], stepped-frequency GPR based on CS is proposed, but it only deals with 2D targets. 3D imaging is the tendency of future GPR, and SFCW-GPR has its own unique advantages as mentioned above. As far as we know, CS has not been applied to 3D SFCW-GPR imaging yet. And, in this paper, 3D imaging method for SFCW-GPR based on CS is discussed.

The paper is organized as follows. Section 2 briefly describes the theory of compressive sensing. The compressive sensing algorithm for stepped frequency GPR and the selection of the related parameters are explained in Section 3. Section 4 presents results for the simulated stepped frequency GPR with a performance analysis. Conclusions are drawn in Section 5.

2. BASIS THEORY OF COMPRESSIVE SENSING

When the object signal is sparse, compressive sensing provides a very efficient sampling method which will significantly decrease the required volume of the collected data. Sparsity means that the number of nonzero coefficients representing a signal in a certain basis is much less than its dimension. Considering a discrete signal vector $\mathbf{x} \in R^N$, we say that it is K-sparse if K ($K \ll N$) of its coefficients are nonzero on an orthonormal basis or over-complete dictionary $\mathbf{\Psi} \in C^{N\times N}$. Hence, the true information is contained in $\mathbf{x}$ which lives at most K dimensions rather than N. The sparse signal can be expressed as

$$\mathbf{x} = \mathbf{\Psi}\boldsymbol{\alpha} \tag{1}$$

where vector $\boldsymbol{\alpha} \in R^{N\times 1}$ is the weighting coefficient. As the signal $\mathbf{x}$ has a sparse representation in $\mathbf{\Psi}$, $\mathbf{x}$ can be well approximated by the best K term expression.

According to CS theory, the measured signal is acquired by linear projections $\mathbf{y} = \Phi\mathbf{x}$. It makes sense that only M samples of signal $\mathbf{x}$ need to be measured instead of N. Then, considering a linear measurements matrix $\mathbf{\Phi} \in C^{M\times N}$ with $M < N$, the measurements signal $\mathbf{y} \in R^M$ is descried as

$$\mathbf{y} = \mathbf{\Phi x} = \mathbf{\Phi\Psi}\boldsymbol{\alpha} = \mathbf{\Theta}\boldsymbol{\alpha} \tag{2}$$

where $\mathbf{\Theta} = \mathbf{\Phi\Psi}$ is a $M \times N$ matrix. This set of equations is underdetermined, and (2) has infinitely many solutions. However, it is indeed possible to recover the sparse signal via CS when the matrix $\mathbf{\Phi}$ has the Restricted Isometry Property (RIP) of order K [16].

Knowing the observed vector $\mathbf{y}$ and the measured matrix $\mathbf{\Theta}$, the signal $\mathbf{x}$ can be recovered from the solution of a convex optimization problem based on l_1 norm

$$\min \|\boldsymbol{\alpha}\|_l \quad st. \ \ \mathbf{y} = \mathbf{\Theta}\boldsymbol{\alpha} \tag{3}$$

If noise is taken into account, the modified convex problem can be described as

$$\min \lambda \|\boldsymbol{\alpha}\|_l \quad st. \quad \|\mathbf{y} - \mathbf{\Theta}\boldsymbol{\alpha}\|_2 \leq \varepsilon \tag{4}$$

where λ is weighted coefficient, and ε bounds the amount of noise in measured data.

3. COMPRESSIVE SENSING FOR 3D SFCW-GPR IMAGING

In the application of GPR, when detecting the ordnances, tubes or metal steels, these small buried targets can be viewed as many discrete

scatter centrals. If the object zone is subdivided, these scatter centers usually take a small part of the space unite, i.e., the image to be reconstructed is sparse, and the precondition of the CS is satisfied. The proposed CS imaging method will make full use of the sparsity of the targets to precisely image the buried targets.

3.1. Construction of the Dictionary Matrix

The two-layer scenario of 3D GPR imaging is shown in Fig. 1. The target space $\boldsymbol{\pi}_{\mathrm{T}}$, which lies in the product space $[x_i x_f] \times [y_i y_f] \times [z_i z_f]$ is discretized into a finite set of N points $\mathbf{B}= \{\boldsymbol{\pi}_1, \boldsymbol{\pi}_2, \ldots, \boldsymbol{\pi}_{\mathrm{N}}\}$. Here, (x_i, y_i, z_i) and (x_f, y_f, z_f) denote the initial and final positions of the target space to be imaged along each axis, and each $\boldsymbol{\pi}_j$ is a 3D vector $[x_j, y_j, z_j]$. The transmit and receive antenna pair, situated at a known height h from the ground/air interface, moves at the step of Δx and Δy along x and y axes, respectively, to form a 2D measurement space. This is a more general and realistic case for 3D imaging, but it is much harder to figure out the received signal of each antenna. As the SFCW-GPR scans a region, at each scan position, the transmitter transmits M continuous sinusoidal signals, sequentially changing the frequencies from the initial frequency f_0 with frequency step Δf.

Suppose that the medium of the ground is uniform and nondispersive, that there are P point-like targets underground, illuminated in the main lobe of the antennas, and that the multi-scattering among the targets do not happen. Then the frequency response measurement at the ith scan position is:

$$\boldsymbol{\xi}_i(\boldsymbol{\omega}) = \sum_{k=1}^{P} \mathbf{b}(k) \exp\left(-j\boldsymbol{\omega}\tau_i(\boldsymbol{\pi}_k)\right) \tag{5}$$

where $\boldsymbol{\omega}$ is the vector of M signal frequencies $\boldsymbol{\omega}_i = 2\pi(f_0 + m\Delta f)$. $m = 0, 1, \ldots, M-1$. $\tau_i(\boldsymbol{\pi}_k)$ denotes the time delay of the signal form

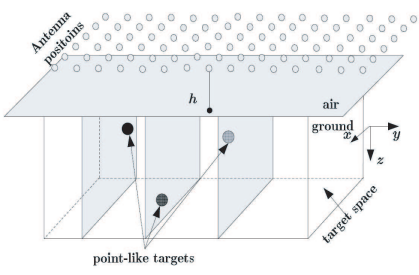

Figure 1. Scenario of 3D GPR imagin.

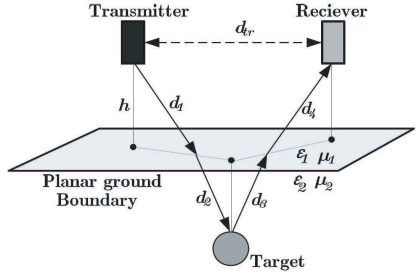

Figure 2. GPR measurement setup of antenna pair.

the transmitter to the target π_k and then reflected to the receiver at ith scan position. $\mathbf{b}$ is a weighed indicator $N \times 1$ vector defining the target space, i.e., if there is a target at π_j, the value of the jth element of $\mathbf{b}$ should be the reflection coefficient σ_j; otherwise, it is zero. Our goal is to find $\mathbf{b}$, which is actually an "image" of the target space.

Equation (5) can be rewrite in the following matrix form

$$\boldsymbol{\xi}_i(\boldsymbol{\omega}) = \boldsymbol{\Psi}_i \mathbf{b} \tag{6}$$

where $\boldsymbol{\Psi}_i$ can be viewed as the dictionary matrix of $M \times N$, the jth column of which, $[\boldsymbol{\Psi}_i]_j$, corresponds to the frequency response of the target at π_j when the GPR is at the ith scan position

$$[\boldsymbol{\Psi}_i]_j = \exp(-j\boldsymbol{\omega}\tau_i(\pi_k)) \tag{7}$$

According to the ray theory view of electromagnetic wave propagation, the transmitted signal follows the path in Fig. 2. At the boundary between two different media (such as air and soil), the direction changes according to Snell's law, but exact calculation of the refraction points requires the solution of a 4 degree polynomial. Several approximations are available in [17]. After finding the reflection points, the distances $d_{1:4}$ can be calculated, and then the time delay $\tau_i(\pi_k)$ can be calculated as follow:

$$\tau_i(\pi_k) = (d_1 + d_4)/v_1 + (d_2 + d_3)/v_2 \tag{8}$$

where v_1 and v_2 are the wave propagation velocities in the air and soil.

3.2. Construction of the Measurement Matrix

Standard SFCW-GPR measures at a fixed set of M frequencies for each scan position, Hence the dimension of $\boldsymbol{\xi}_i(\boldsymbol{\omega})$ is $M \times 1$. By compressive sensing sampling data acquisition method, a very small number of "random" measurements carry enough information to reconstruct the buried targets. Thus, a subset of L frequencies for each scan position is measured. In the matrix form, the new measurements $\boldsymbol{\beta}_i$ can be written as:

$$\boldsymbol{\beta}_i = \boldsymbol{\Phi}_i \boldsymbol{\xi}_i = \boldsymbol{\Phi}_i \boldsymbol{\Psi}_i \mathbf{b} \tag{9}$$

where $\boldsymbol{\Phi}_i$ is a $L \times M$ measurement matrix constructed by randomly selecting L rows of an $M \times M$ identity matrix. This reduces the data acquisition time by L/M.

For each scan position, the measurement matrix may be different or keep the same. In [13], it is proved by simulation that they are the same for the through-wall radar imaging, but the latter is easier for hardware implementation.

3.3. Compressive 3D SFCW-GPR Imaging

As mentioned above, SFCW-GPR needs measurements at different scan positions. For 3D imaging, the transmitter and receiver antenna pair moves along x and y axes to form a 2D grid measurement space. By the compressive sensing imaging method, we just randomly select K scan positions to form a composite dictionary matrix $\boldsymbol{\Psi} = [\boldsymbol{\Psi}_1^T, \boldsymbol{\Psi}_2^T, \ldots, \boldsymbol{\Psi}_K^T]^T$ composite measurement matrix $\boldsymbol{\Phi} = \text{diag}\{\boldsymbol{\Phi}_1, \boldsymbol{\Phi}_2, \ldots, \boldsymbol{\Phi}_K\}$ and the measurement vector $\boldsymbol{\beta} = [\boldsymbol{\beta}_1^T, \boldsymbol{\beta}_2^T, \ldots, \boldsymbol{\beta}_{\mathrm{K}}^T]^T$. Then the recovery of $\mathbf{b}$ is done by solving a constrained l_1 minimization problem

$$\hat{b} = \text{argmin } \|\mathbf{b}\|_{l_1} \quad s.t.\ \boldsymbol{\beta} = \boldsymbol{\Phi}\boldsymbol{\Psi}\mathbf{b} \tag{10}$$

The equality constraints in above equation are only valid for the noiseless case. Generally, the data are always contaminated by the noise in real measurements. Then constraints are as follow

$$\boldsymbol{\beta} = \boldsymbol{\Phi}\boldsymbol{\Psi}\mathbf{b} + \mathbf{n} \tag{11}$$

where $\mathbf{n}$ is the noise vector, following a normal distribution with mean zero and standard deviation σ^2, i.e., $\mathbf{n} \sim \mathcal{N}(0, \sigma^2)$. The reconstruction of the image $\hat{\mathbf{b}}$ is by solving a modified convex optimization problem, called Dantzig Selector [18].

$$\hat{\mathbf{b}} = \text{argmin } \|\mathbf{b}\|_{l_1} \quad s.t.\ \left\|\mathrm{A}^{\mathrm{T}}(\boldsymbol{\beta} - \mathbf{A}\mathbf{b})\right\|_{\boldsymbol{\infty}} < \varepsilon \tag{12}$$

where $\mathbf{A} = \boldsymbol{\Phi}\boldsymbol{\Psi}$, $\boldsymbol{\varepsilon}$ is the amount of noise in measured data. The choice of ε is noise dependent, and selection $\varepsilon = \sqrt{2\sigma^2 \log(KL)}$ makes the true $\hat{\mathbf{b}}$ feasible with high probability [18].

4. SIMULATION RESULTS

In this section, several simulated data results for CS method are presented. It should be mentioned that this paper is mainly focused on CS imaging, aimed at saving data processing time by sampling less data. Before using CS, some data preprocessing methods in [7, 19–21] can be used to remove the ground reflecting effects.

First, to illustrate the random frequency sampling and random antenna position selection idea, a 3D homogenous target space of size 10 cm × 10 cm × 8 cm containing three randomly placed point like targets (suppose $P_1(8, 5, 6)$, $P_2(5, 6, 3)$ and $P_3(5, 8, 4)$) with reflection coefficients 1.0, 0.6 and 0.8 respectively are considered. The target space is discredited into 10 × 10 × 8 points. Bistatic antenna pairs with a 2 cm transmitter-receiver spacing at the height of 10 cm collect frequency domain measurements at frequencies from 100 MHz to

10 GHz with 100 MHz frequency step. Thus, at each scan position, 100 frequency measurements are collected. The antenna pair moves with the step of $\Delta x = \Delta y = 1$ cm along x and y axes, respectively, in the measurement space with the size of 15 cm $\times$ 15 cm. So there are totally 225 positions. The permittivity of the soil ε_r is supposed to be 4, i.e., the signal transmitting velocity in the soil $v_2 = v_1/\sqrt{\varepsilon_r} = 0.5v_1$. For the numerical solution of the l_1-*norm* minimization problems in

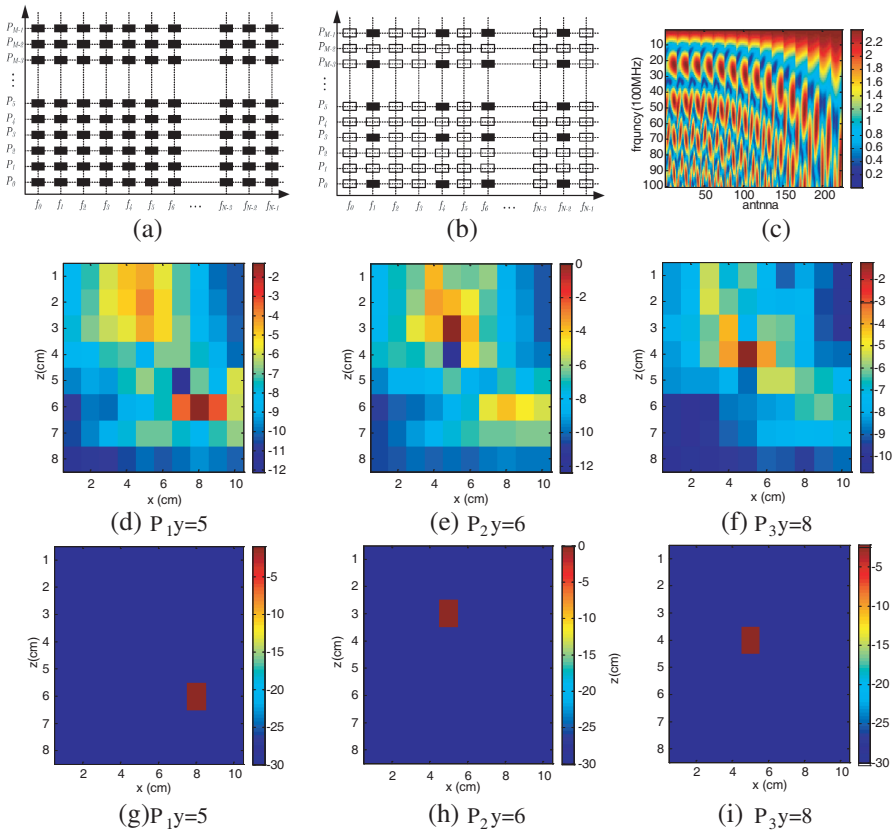

Figure 3. (a) DSBF data acquisition. (b) CS data acquisition where the black points indicates the randomly sampled data when about 7% of the total measurements are used. (c) Noiseless space-frequency domain target response for all the frequency and antenna positions. (d)–(f) DBSF imaging with the full set of data for P_1, P_2, P_3 at $y = 5$, 6, 8 respectively. (g)–(i) CS imaging with randomly selected subset of data for P_1, P_2, P_3 at $y = 5$, 6, 8 respectively.

CS, a convex optimization package called CVX [22] is used. All the simulations are done on a computer with 1.6 GHz Pentium 4 processor and 1G memory.

For the CS method, we use the measurement strategy proposed in [13], which is easy for hardware implementation, i.e., instead of measuring all 100 frequencies at all 225 scan positions, a random subset of 50 positions is firstly selected, and then for each position, the same random subset of 30 frequencies is measured. To make a comparison, the conventional delay-and-sum beam forming (DSBF) algorithm [13], which performs coherent summation of full 100×225 sensor data, is used. The target space slice images at $y = 5$, 6, 8 in Figs. 3(d)–(f) and (g)–(i), the noiseless full space-frequency domain measured data in Fig. 3(a), and the randomly selected space-frequency domain measured data in Fig. 3(b) are shown respectively. It can be seen that when applying CS, much less data are used.

For the DSBF imaging in Figs. 3(d)–(f), it can be seen that the three targets can be seen clearly with small "blobs" in the right

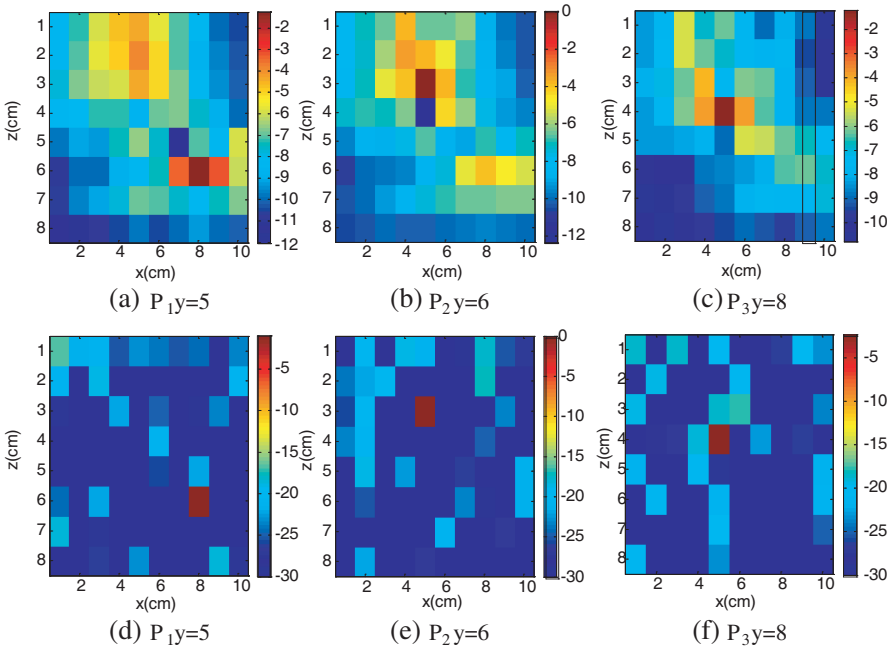

Figure 4. Imaging with 10% additive Gaussian white noise. (a)–(c) DBSF imaging with the full set of data for P_1, P_2, P_3 at $y = 5$, 6, 8 respectively. (d)–(f) CS imaging with randomly selected subset of data for P_1, P_2, P_3 at $y = 5$, 6, 8 respectively.

position, but for Fig. 3(d), a false point-like target at $(5, 5, 2)$ is also imaged. As seen in Figs. 3(g)–(h), while using a much small subset of data, the CS method can recover the targets with much less cluttered image, which is better than DSBF method using the full data set.

Note that in real applications, the measured data are always contaminated with noise. Next, the performance of the algorithm with noise is disused.

4.1. Performance in Noise

To analyze the impact of noise data on the imaging, 10% Gaussian white noise is added to the signal reflected by the above three point-like targets. All other parameters are kept the same with above experiment. The images are shown in Fig. 4.

From the simulation result shown in Fig. 4, with the additives noise, though there is a subtle change for DSBF images the clutters and false targets still exist. Whereas, for the CS method, there are some changes, more clusters appear, but except the targets, the values of the

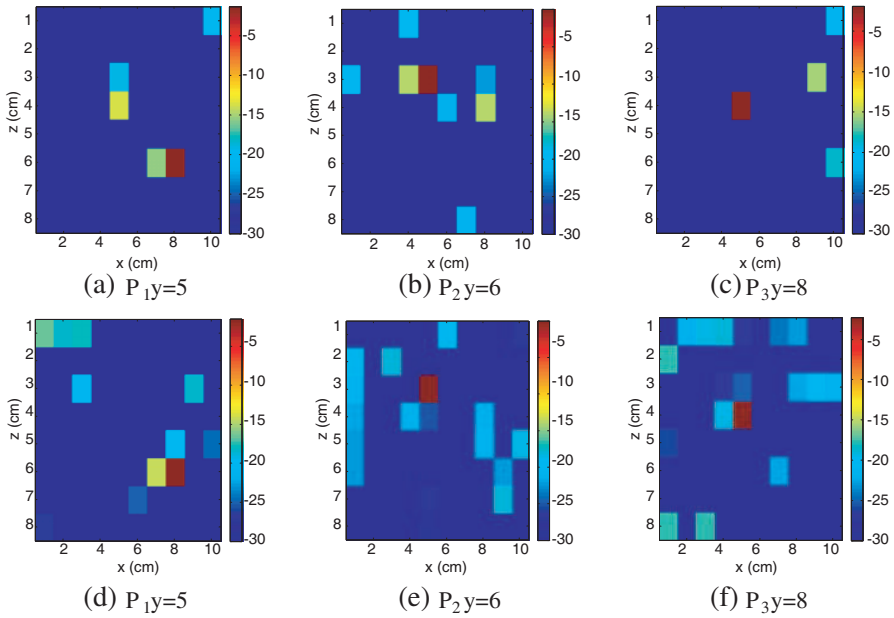

Figure 5. CS imaging with different bandwidth. (a)–(c) CS imaging with bandwidth of 2 [1–3] GHz for P_1, P_2, P_3 at $y = 5$, 6, 8 respectively. (d)–(f) CS imaging with bandwidth of 5 [0.5–5.5] GHz for P_1, P_2, P_3 at $y = 5$, 6, 8 respectively.

pixels are all less than 15 dB which can be viewed as the background, i.e., the targets are all at the right position, and no false targets appear.

4.2. Effect of Bandwidth

The bandwidth of the measured frequency spectrum is an important parameter in the SFCWGPR. To analyze the effect of frequency bandwidth on the imaging, in this subsection, different bandwidths of 2 GHz and 5 GHz are tested for the above three point-like targets. In the simulation, 10% noise is added. The images are shown in Fig. 5.

It can be observed in Fig. 5 that the CS method is able to reconstruct the true target points even for the low bandwidth of 2 GHz. Besides, with smaller bandwidth, the number of "false target points" becomes smaller, but with stronger intensity.

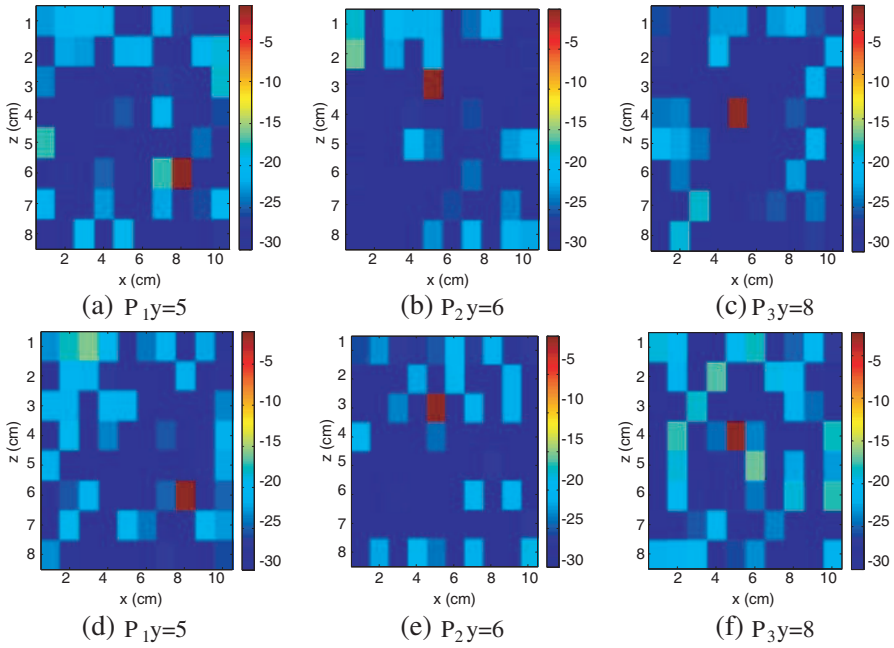

Figure 6. CS imaging with different wave travel velocity in soil and 10% additive Gaussian white noise. The true wave travel velocity in soil is $v = 1.5 \times 10^8$ m/s. (a)–(c) Wave travel velocity in soil $v = 1.7321 \times 10^8$ m/s for P_1, P_2, P_3 at $y = 5$, 6, 8 respectively. (d)–(f) wave travel velocity in soil $v = 1.3416 \times 10^8$ m/s for P_1, P_2, P_3 at $y = 5$, 6, 8 respectively.

4.3. Effect of the Wave Travel Velocity Estimation Error

In above simulations, we view the wave travel velocity in soil as a known parameter. However, in most of the real applications, it is unknown or has a measurement error from the true value, which will directly affect the imaging. In this subsection, the effect of the wave travel velocity estimation error is discussed. The true velocity is $15 \times 108\,\mathrm{m/s}$ ($\varepsilon_r = 4$). In the simulation, the measured data are sampled using the true velocity, and the dictionary matrix is calculated using the estimated velocity of $1.7321 \times 108\,\mathrm{m/s}$ ($\varepsilon_r = 3$) and $1.3416 \times 108\,\mathrm{m/s}$ ($\varepsilon_r = 5$), respectively. The other parameters are kept the same in the second simulation. The images are shown in Fig. 6.

Figure 6 shows that even if the wave travel velocity in soil is wrongly estimated to some extent, the targets can still be correctly imaged by the CS method, because in spite of certain difference between the dictionary matrix constructed by the true velocity and the one constructed by the estimated velocity, CS is based on the l_1 *norm* optimization. By solving the convex optimization, the true image can be reconstructed.

5. CONCLUSION

This work deals with the imaging of the three dimensional buried point-like targets based on the compressive sensing method. By solving the constrained convex optimization problem, the targets can be recovered with much less sampled data, which will save the data collecting time. Even with 10% additive noise, smaller bandwidth and some wave travel velocity estimation error, the image of the targets can be reconstructed with little degradation. Further work will be exerted on the application of CS to small 3D block-like targets imaging of SFCWGPR.

ACKNOWLEDGMENT

This work was supported by the National Key Laboratory of Millimeter Waves at Southeast University in China (No. K20121) and the Natural Science Foundation of Shanxi Province, China (No. 2011JM8025).

REFERENCES

1. Grandjean, G., J. Gourry, and A. Bitri, "Evaluation of GPR techniques for civil-engineering applications: Study on a test site," *J. Appl. Geophys.*, Vol. 45, No. 3, 141–156, 2000.

2. Feng, X. and M. Sato, "Pre-stack migration applied to GPR for landmine detection," *Inverse Prob.*, Vol. 20, 99–115, 2004.
3. Groenenboom, J. and A. Yarovoy, "Data processing and imaging in GPR system dedicated for landmine detection," *Subsurf. Sens. Technol. Appl.*, Vol. 3, No. 4, 387–402, 2002.
4. Hubbard, S., C. Jinsong, K. Williams, Y. Rubin, and J. Peterson, "Environmental and agricultural applications of GPR," *Proc. 3rd Int. Workshop on Adv. Ground Penetrating Radar*, 45–49, 2005.
5. Daniels, D., *Ground Penetrating Radar*, 2nd edition, London, UK, 2004.
6. Counts, T., A. C. Gurbuz, W. R. Scott, Jr., J. H. McClellan, and K. Kangwook, "Multistatic ground-penetrating radar experiments," *IEEE Trans. Geosci. Remote Sens.*, Vol. 45, No. 8, 2544–2553, Aug. 2007.
7. Lopera, O., E. C. Slob, N. Milisavljevic, and S. Lambot, "Filtering soil surface and antenna effects from GPR data to enhance landmine detection," *IEEE Trans. Geosci. Remote Sens.*, Vol. 45, No. 3, 707–717, 2007.
8. Fang, G.-Y. and M. Sato, "Stepped frequency ground penetrating radar and its application for landmine detection," *Acta Electronica Sinica*, Vol. 33, No. 3, 436–439, 2005.
9. Gurbuz, A. C., J. H. McClellan, and W. R. Scott, "A compressive sensing data acquisition and imaging method for stepped frequency GPRs," *IEEE Transactions on Signal Processing*, Vol. 57, No. 7, 2640–2650, 2009.
10. Donoho, D. L., "Compressive sensing," *IEEE Trans. on Information. Theory*, Vol. 52, No. 4, 1289–1306, 2006.
11. Baraniuk, R. and P. Steeghs, "Compressive radar imaging," *Proc. IEEE Radar Conf.*, 128–133, 2007.
12. Yu. H.-M. and Y. Fang, "Research on compressive sensing based 3D imaging method applied to ground penetrating radar," *Journal of Electronics & Information Technology*, Vol. 32, No. 1, 12–16, 2010.
13. Huang, Q., L. Qu, B. Wu, and G. Fang, "UWB through-wall imaging based on compressive sensing," *IEEE Trans. Geosci. Remote Sens.*, Vol. 48, No. 3, 1408–1415, 2010.
14. Wei, S.-J., X.-L. Zhang, J. Shi, and G. Xiang, "Sparse reconstruction for SAR imaging based on compressed sensing," *Progress In Electromagnetics Research*, Vol. 109, 63–81, 2010.
15. Zhang, L., M. Xing, C. Qiu, et al., "Achieving higher resolution ISAR imaging with limited pulses via compressed sampling,"

IEEE Geoscience and Remote Sensing Letters, Vol. 6, No. 3, 567–571, 2009.

16. Candes, E. J. and M. Wakin, "An introduction to compressive sampling," *IEEE Signal Processing Magazine*, 2130, Mar. 2008.
17. Johansson, E. M. and J. E. Mast, "Three dimensional ground penetrating radar imaging using a synthetic aperture time-domain focusing," *Proc. SPIE Conf. Adv. Microw. Millimeter Wave Detectors*, Vol. 2275, 205–214, 1994.
18. Candes, E. and T. Tao, "The Dantzig selector: Statistical estimation when p is much larger than n," *Ann. Statist.*, Vol. 35, No. 6, 2313–2351, 2007.
19. Tuncer, M. A. C. and A. C. Gurbuz, "Ground reflection removal in compressive sensing ground penetrating radars," *IEEE Geoscience and Remote Sensing Letters*, 2011.
20. Picardi, M., "Background subtraction techniques — A review," *Proc. IEEE Int. Conf. Syst. Man. Cybern.*, 3099–3104, Oct. 10–13, 2004.
21. Mayordomo, A. M. and A. Yarovoy, "Optimal background subtraction in GPR for humanitarian demining," *Proc. 5th Eur. Radar Conf.*, 48–51, Oct. 2008.
22. Grant, M. and S. Boyd, CVX: Matlab Software for Disciplined Convex Programming (Web Page and Software), 2011, Available: http://stanford.edu/ boyd/cvx.